

Cooperative Nature of Ferroelectricity in Two-Dimensional Hybrid Organic–Inorganic Perovskites

Yali Yang, Feng Lou, and Hongjun Xiang*



Cite This: *Nano Lett.* 2021, 21, 3170–3176



Read Online

ACCESS |



Metrics & More



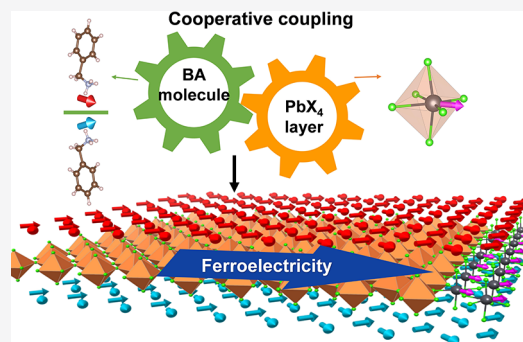
Article Recommendations



Supporting Information

ABSTRACT: Two-dimensional (2D) ferroelectric (FE) hybrid organic–inorganic perovskites (HOIPs) are promising for potential applications as miniaturized flexible ferroelectric/piezoelectric devices. Recently, several 2D HOIPs [e.g., Ruddlensden–Popper type HOIP BA_2PbCl_4 ($\text{BA} = \text{C}_6\text{H}_5\text{CH}_2\text{NH}_3^+$)] were reported to possess room-temperature ferroelectricity. However, the underlying microscopic mechanisms for ferroelectricity in 2D HOIPs remain elusive. Here, by performing first-principles calculations and symmetry mode analysis, we demonstrate that there exists a cooperative coupling between A-site organic molecules and B-site inorganic Pb^{2+} ions that is essential to the ferroelectricity in 2D BA_2PbCl_4 . The nonpolar ground state of the closely related compounds BA_2PbBr_4 and BA_2PbI_4 can also be explained in terms of the weakened cooperative coupling. We further predict that 2D BA_2PbF_4 displays in-plane ferroelectricity with a higher Curie temperature and larger electric polarization. Our work not only reveals the unusual FE mechanism in 2D HOIPs but also provides a solid theoretical basis for the rational design of 2D multifunctional materials.

KEYWORDS: two-dimensional ferroelectric, hybrid organic–inorganic perovskites, first-principles calculations, symmetry mode analysis, cooperative coupling



Hybrid organic–inorganic perovskites (HOIPs) have gained much attention because of their structural diversity, low cost of manufacture, ease of fabrication, and remarkable properties.^{1–11} Comparing to 3D HOIPs, two-dimensional (2D) layered HOIPs not only break the strict restrictions of the tolerance factor concept and thus show a greater structure tunability but also show much better environmental stability in air and light.^{12–15} Furthermore, 2D HOIPs display unique physical properties including strong light harvesting capability, efficient photoluminescence intensity, nonlinear optical properties, and large exciton binding energy.^{16,17} Therefore, 2D HOIPs are emerging as an important member of 2D soft functional materials.

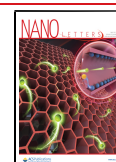
As one of the important properties, ferroelectricity was observed in a number of 2D layered Ruddlensden–Popper (RP) type HOIPs ($\text{A}_{n+1}\text{B}_n\text{X}_{3n+1}$ composition).^{18–27} Notably, the thinnest RP type (i.e., the $n = 1$ A_2BX_4 series) van der Waals (vdW) material BA_2PbCl_4 ($\text{BA} = \text{C}_6\text{H}_5\text{CH}_2\text{NH}_3^+$, benzylammonium) is found to possess robust room-temperature in-plane ferroelectricity.^{18,28} At high temperature, BA_2PbCl_4 adopts paraelectric symmetry $I4/mmm$ with disordered organic cations.²⁹ As temperature decreases below the ferroelectric (FE) Curie temperature T_c (about 438 K), it crystallizes into a noncentrosymmetric space group $\text{Cmc}2_1$. The measured ferroelectric polarization is as high as $P = 8\text{--}13 \mu\text{C}/\text{cm}^2$,^{18,28} which is among the highest values observed for molecular and HOIP ferroelectrics. Owing to the weak vdW

interlayer interactions, the in-plane ferroelectricity was found to survive at room temperature in ultrathin films down to two PbCl_4 layers with a thickness of 3.4 nm.²⁸ The structural flexibility and room-temperature ferroelectricity make 2D BA_2PbCl_4 highly promising for flexible electromechanical applications. However, the origin of ferroelectricity in BA_2PbCl_4 remains elusive. First, although 2D layered BA_2PbCl_4 displays a FE ground state, the closely related compounds BA_2PbBr_4 and BA_2PbI_4 are found to adopt nonpolar ground states.^{18,30} Second, the so-called hybrid improper mechanism³¹ that accounts for the in-plane ferroelectricity in the $n = 2$ inorganic RP perovskites $\text{Ca}_3\text{B}_2\text{O}_7$ ($\text{B} = \text{Ti}, \text{Mn}$)^{32,33} is not applicable to the $n = 1$ RP perovskites A_2BX_4 (both inorganic and hybrid) systems. In fact, the inorganic RP A_2BX_4 materials, e.g., Sr_2IrO_4 ,³⁴ tend to crystallize into nonpolar ground structures.^{35–37} Third, it was widely believed that the ferroelectricity in HOIPs originates from the order–disorder of molecules.^{38,39} Does the inorganic framework play a significant role on ferroelectricity given the

Received: January 30, 2021

Revised: March 12, 2021

Published: March 23, 2021



ACS Publications

© 2021 American Chemical Society

3170

<https://doi.org/10.1021/acs.nanolett.1c00395>
Nano Lett. 2021, 21, 3170–3176

fact that most of the FE HOIPs contain Pb^{2+} ions at the B-sites.^{28,40,41} Therefore, it is urgent to clarify the mechanism of ferroelectricity in 2D HOIPs and address how to design 2D high-performance HOIP ferroelectrics.

In this Letter, we propose an exact but simple method for investigating mode interactions. With this new method, we reveal the cooperative coupling between the organic molecules and inorganic framework in HOIPs which not only explains the ferroelectricity in layered BA_2PbCl_4 but also stimulates us to predict that 2D BA_2PbF_4 is a FE with a larger polarization and higher T_c .

We first do density functional theory (DFT) calculations on bulk BA_2PbCl_4 and its bilayer thin film (see sections II–IV of the Supporting Information), the results show that bulk BA_2PbCl_4 has a FE ground structure and the ferroelectricity can survive in its bilayer thin film, in agreement with the experimental results.^{18,28}

Now we turn to the case of the thinnest film of BA_2PbCl_4 , i.e., the monolayer case. In order to reliably predict the ground state structure, we first “exfoliate” the layered FE bulk BA_2PbCl_4 to obtain a FE monolayer structure with the space group $Pb2_1m$; then we perform the ab-initio random structure searching (AIRSS) (see section V of the Supporting Information).⁴² We find that the FE structure with the $Pb2_1m$ symmetry has the lowest total energy (see Figure 1a). In addition, we find a metastable AFE structure with the $P2_1/c$ symmetry (see Figure 1b), which is higher in energy by 7.2 meV/f.u. than the FE state. For each BA cation in both FE and AFE states, the head $-\text{C}_6\text{H}_5$ of the BA cation directs toward to the out-of-plane direction, while the tail $-\text{CH}_2\text{NH}_3$ sits into the interval of four neighboring PbCl_6 octahedrons. Hereafter,

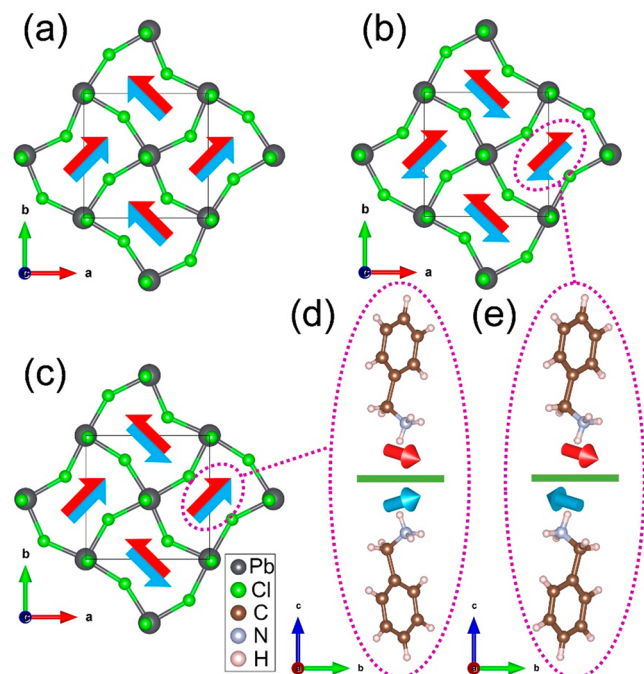


Figure 1. Structure diagram of BA_2PbCl_4 monolayer. (a) FE ground state, (b) AFE state, and (c) metastable FE state from the top view. (d) Parallel and (e) antiparallel alignment of BA cations from the side view. The red and blue arrows indicate the orientations of the C–N dipole of BA cations at the top and bottom layer, respectively. The inorganic frameworks in (d) and (e) are indicated by the green line for clarity.

we characterize the orientation of the BA cation with the direction of the C–N dipole of $-\text{CH}_2\text{NH}_3$. As shown in Figure 1a, all the BA cations in the FE state align with a net nonzero C–N dipole along the $[010]$ direction (see Figure 1d). In the AFE state, the two layers of BA cations slant to opposite directions, which leads to the cancellation of C–N dipoles (see Figure 1e). From our above AIRSS, we find that in low-energy structures, a given BA cation can only orient toward two opposite directions (i.e., the directions with more empty space resulting from the out-of-plane rotation of PbCl_6 octahedra). This is because of the well-known steric effect. By enumerating all plausible orientations of C–N dipoles, we obtain 16 different configurations in total (see Figure S4 of the Supporting Information). After optimizing these configurations, we get three symmetrically inequivalent states: the FE state with the $Pb2_1m$ symmetry with the lowest total energy (see Figure 1a); the AFE state with the $P2_1/c$ symmetry (see Figure 1b); the metastable FE state with the net C–N dipoles along the $[110]$ direction and with a higher energy by 3.3 meV/f.u. than the FE state (see Figure 1c). Furthermore, we confirm the thermodynamic stability of the FE BA_2PbCl_4 monolayer by calculating the decomposition energy (see section V of the Supporting Information). Our band structure calculations indicate that the FE BA_2PbCl_4 monolayer has a large band gap about 3.32 eV, in agreement with experimental result of 3.65 eV.¹⁸ Therefore, we conclude that BA_2PbCl_4 monolayer is ferroelectric.

As shown in Figure S5, the electric polarization of BA_2PbCl_4 monolayer is evaluated to be $5.65 \mu\text{C}/\text{cm}^2$ along the $+b$ -axis, in agreement with a recent computational study.⁴³ For comparison, the polarization of the FE bulk BA_2PbCl_4 structure is calculated to be about $6.08 \mu\text{C}/\text{cm}^2$ along the $+b$ -axis, which is close to the experimental value of $8\text{--}13 \mu\text{C}/\text{cm}^2$ measured by different methods at different temperatures.^{18,28} The reason for the underestimation may have several source of errors.⁴³ Our results suggest that one can optimize the polarization of a bulk vdW crystal by focusing on the polarization of the monolayer building block. In order to investigate the individual contributions from different functional units, i.e., organic cations and inorganic framework, we adopt the so-called functional-unit mode analysis, which was used successfully for the analysis of FE polarization in hybrid compounds.^{44,45} Our analysis shows that the polarization contains two main contributions of the similar magnitude, one is from the ordering of organic dipole about $3.95 \mu\text{C}/\text{cm}^2$, and the other part (about $1.70 \mu\text{C}/\text{cm}^2$) comes from the Pb off-center displacement. Therefore, BA_2PbCl_4 monolayer is an unusual 2D ferroelectric with both order–disorder and displacive characteristics.

There has been a hot debate whether the ferroelectricity in HOIPs originates either from the organic molecules or from the inorganic framework.^{28,44,46,47} Therefore, now let us focus on the microscopic mechanism of ferroelectricity in BA_2PbCl_4 . We first neglect the strain effect, because our tests (see section VII of the Supporting Information) indicate that the strain effect is not critical to the FE ground state of BA_2PbCl_4 . Then, we perform mode decomposition for the FE state of the BA_2PbCl_4 monolayer with respect to the high symmetry parent (PE) $P2_1/c$ phase (see Figure 2). Comparing to the AFE structure in Figure 1b, the PE structure has the same alignment of BA cations, while there is no rotation of PbCl_6 octahedra in the inorganic framework (see Figure 2b). We note that the rotation of organic BA cations in the FE state is treated as an

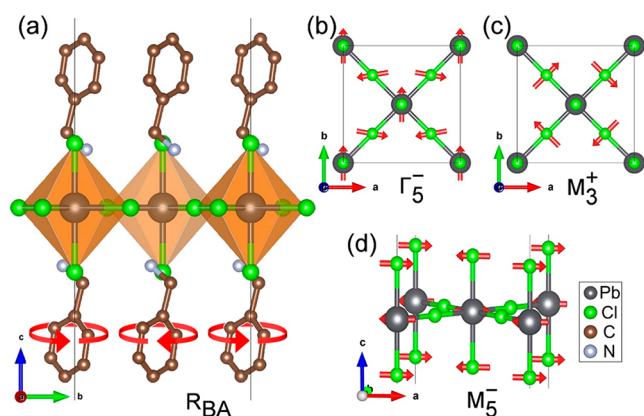


Figure 2. Symmetry mode decompositions for the FE BA_2PbCl_4 monolayer. (a) BA cation rotation mode R_{BA} , (b) FE displacement mode Γ_5^- , (c) octahedral rotation mode M_3^+ , and (d) AFE displacement mode M_5^- . The red arrows in (a) represent the rotation of BA cation, and in (b)–(d) they represent the direction of atomic displacements. The hydrogen atoms in (a), as well as the BA cations in (b)–(d), are not shown for clarity. Note that only one layer of BA molecule rotates in the R_{BA} mode.

out-of-plane rotation mode (indicated by R_{BA}) with respect to the PE state (see Figure 2a). As for the PbCl_4 framework, we find that the FE phase has three dominant distortions: the FE

displacement mode with the irreducible representation (irrep) Γ_5^- (see Figure 2b), the out-of-plane octahedral rotation mode with irrep M_3^+ (see Figure 2c), and the AFE displacement mode with irrep M_5^- (see Figure 2d).

For the purpose of investigating the interplay between different modes in FE state, we first compute the total energies as the function of the amplitude of the four individual modes (namely, R_{BA} , Γ_5^- , M_3^+ , M_5^-) relative to the PE structure (see Figure 3a). For the two AFE distortions, the sole presence of the M_5^- mode is unstable and lifts the total energy by about 87.51 meV/f.u., but the octahedral rotation mode M_3^+ is extremely favored, which can significantly lower the total energy by about 448.03 meV/f.u. The instability of the M_3^+ mode may be related to the size and shape of the BA ions. For the two FE modes, one can see that with the rotation of BA dipole from AFE to FE alignment, the total energy increases by about 30.15 meV/f.u. Similarly, the sole presence of the Γ_5^- mode results in an increase of total energy by about 9.98 meV/f.u. It is interesting that the two FE distortions are unfavored while the FE state is the ground state in the BA_2PbCl_4 monolayer. Therefore, there must exist strong couplings between different modes to lower the total energy of the FE ground state. To find out the relevant coupling terms, we consider the expression of the total energy as the function of the above-mentioned distortion modes:

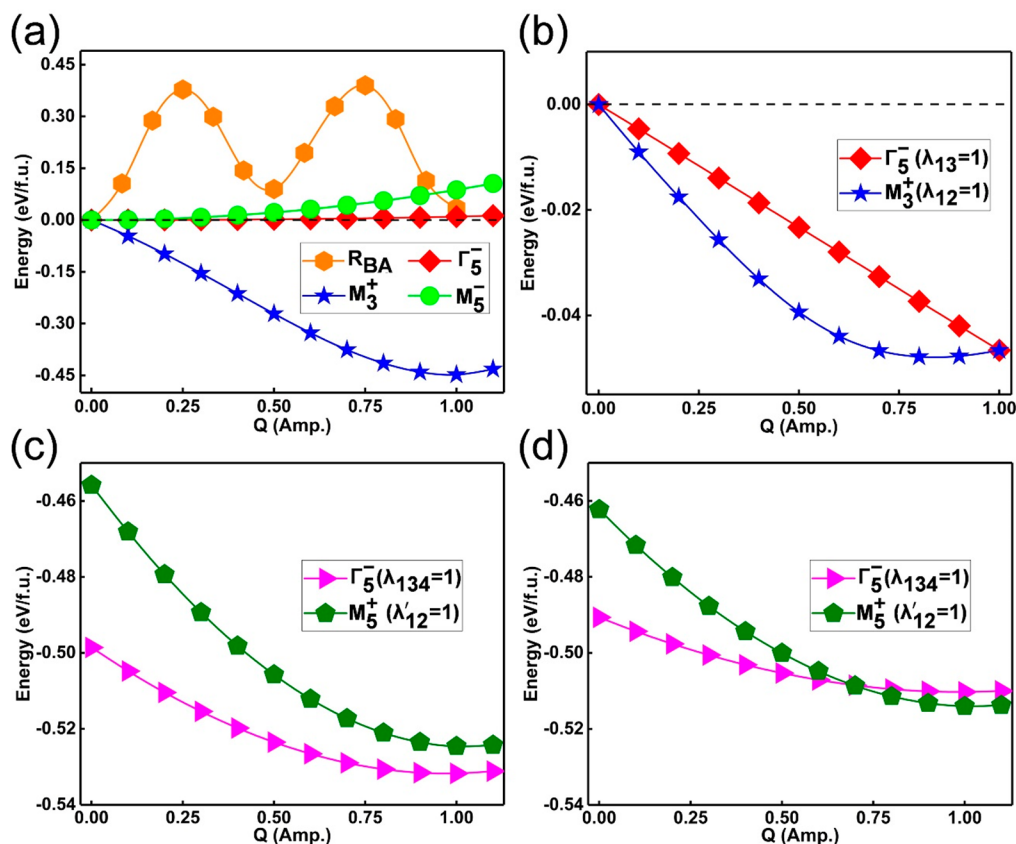


Figure 3. Total energies as a function of symmetry modes. (a) Total energies as a function of symmetry mode in the FE BA_2PbCl_4 monolayer. (b) Contributions of $E_1^{\text{III}}(R_{\text{BA}}, \Gamma_5^-, M_3^+)$ to the total energy as a function of Γ_5^- and M_3^+ modes in the FE BA_2PbCl_4 monolayer. $\lambda_{13} = 1$ depicts the amplitudes $Q(R_{\text{BA}}) = 1$ and $Q(M_3^+) = 1$. $\lambda_{12} = 1$ depicts $Q(R_{\text{BA}}) = 1$ and $Q(\Gamma_5^-) = 1$. (c) Total energies as a function of the Γ_5^- mode and M_3^+ mode in the BA_2PbCl_4 monolayer. (d) Total energies as a function of the Γ_5^- and M_5^- modes in the BA_2PbBr_4 monolayer. $\lambda_{134} = 1$ depicts the amplitudes $Q(R_{\text{BA}}) = 1$, $Q(M_3^+) = 1$, and $Q(M_5^-) = 1$ for the FE monolayer structure. $\lambda'_{12} = 1$ depicts $Q(M_3^+) = 1$ and $Q(\Gamma_5^-) = 1$ for the AFE monolayer structure.

Table 1. Energy Difference $\Delta E = E_{\text{AFE}} - E_{\text{FE}}$ (meV/f.u.) and Amplitude of the Symmetry Modes (\AA) in the BA_2PbX_4 ($\text{X} = \text{F}, \text{Cl}, \text{Br}, \text{and I}$) Monolayer Structure

		BA_2PbF_4	BA_2PbCl_4	BA_2PbBr_4	BA_2PbI_4
	ΔE	39.6	7.2	−4.7	−34.3
FE monolayer	Γ_5^- (FE)	0.503	0.321	0.243	0.192
	M_3^+ (AFE)	1.462	1.683	1.659	1.792
	M_5^- (AFE)	0.595	0.245	0.245	0.134
AFE monolayer	Γ_3^+ (AFE)	0.399	0.090	0.042	0.031
	M_3^+ (AFE)	1.507	1.658	1.636	1.761
	M_5^+ (AFE)	0.711	0.337	0.311	0.265

$$\begin{aligned}
 E_{\text{FE}} &= E_{\text{PE}} + E^{\text{I}} + E^{\text{II}} + E^{\text{III}} + E^{\text{IV}} \\
 E^{\text{I}} &= E_1^{\text{I}}(\text{R}_{\text{BA}}) + E_2^{\text{I}}(\Gamma_5^-) + E_3^{\text{I}}(M_3^+) + E_4^{\text{I}}(M_5^-) \\
 E^{\text{II}} &= E_1^{\text{II}}(\text{R}_{\text{BA}}, \Gamma_5^-) + E_2^{\text{II}}(\text{R}_{\text{BA}}, M_3^+) + E_3^{\text{II}}(\text{R}_{\text{BA}}, M_5^-) \\
 &\quad + E_4^{\text{II}}(\Gamma_5^-, M_3^+) + E_5^{\text{II}}(\Gamma_5^-, M_5^-) + E_6^{\text{II}}(M_3^+, M_5^-) \\
 E^{\text{III}} &= E_1^{\text{III}}(\text{R}_{\text{BA}}, \Gamma_5^-, M_3^+) + E_2^{\text{III}}(\text{R}_{\text{BA}}, \Gamma_5^-, M_5^-) \\
 &\quad + E_3^{\text{III}}(\text{R}_{\text{BA}}, M_3^+, M_5^-) + E_4^{\text{III}}(\Gamma_5^-, M_3^+, M_5^-) \\
 E^{\text{IV}} &= E_1^{\text{IV}}(\text{R}_{\text{BA}}, \Gamma_5^-, M_3^+, M_5^-)
 \end{aligned}
 \tag{1}$$

where E_{FE} and E_{PE} are the total energies of the FE and PE phases, respectively. The energy difference between the FE and PE phases includes four one-body terms (E^{I}), six two-body interaction terms (E^{II}), four three-body interaction terms (E^{III}), and one four-body interaction term (E^{IV}). To extract the individual contributions, we propose an exact method (see section VII of the Supporting Information for details). In brief, we calculate the total energies of 16 structures in which the amplitude (Q) of these four modes is set to 1 (i.e., the mode amplitude of the FE state with respect to the PE state) or 0. The contributions of each energy terms can then be extracted using these 16 total energies. As shown in Table S1 of the Supporting Information, we find that the two-body interactions $E_2^{\text{II}}(\text{R}_{\text{BA}}, M_3^+)$ and $E_3^{\text{II}}(\text{R}_{\text{BA}}, M_5^-)$ and three-body interaction $E_1^{\text{III}}(\text{R}_{\text{BA}}, \Gamma_5^-, M_3^+)$ can significantly lower the total energy by about 43.61, 135.77, and 46.62 meV/f.u., respectively. Our results indicate that the presence of the FE mode R_{BA} can be ascribed to the two-body interactions with the M_3^+ and M_5^- modes. Meanwhile, the presence of the FE mode Γ_5^- can be mainly ascribed to its three-body interaction with the R_{BA} and M_3^+ modes. Our results therefore show that there exists a cooperative coupling between organic dipole and inorganic framework in BA_2PbCl_4 monolayer. In order to better understand the cooperative coupling term involving the organic molecule FE R_{BA} mode and the Pb related FE mode Γ_5^- , we calculate the three-body interaction $E_1^{\text{III}}(\text{R}_{\text{BA}}, \Gamma_5^-, M_3^+)$ as a function of Γ_5^- and M_3^+ modes (see Figure 3b). One can see that $E_1^{\text{III}}(\text{R}_{\text{BA}}, \Gamma_5^-, M_3^+)$ is proportional to the amplitude of the Γ_5^- mode, while for the M_3^+ mode, its contribution includes not only a linear component but also the nonlinear component when the M_3^+ mode is large. We note that without the three-body interaction $E_1^{\text{III}}(\text{R}_{\text{BA}}, \Gamma_5^-, M_3^+)$, the FE state would have a higher energy than the AFE state. Therefore, we demonstrate that the cooperative coupling between the A-site organic dipole and inorganic framework is the origin of ferroelectricity in the BA_2PbCl_4 monolayer.

The similar mode decomposition and the corresponding energy decomposition are also performed for the AFE state of BA_2PbCl_4 monolayer (see section VIII of the Supporting

Information). We find that although the individual modes and their interactions significantly stabilize the AFE state with respect to the PE state; nevertheless, the AFE state still has a higher energy by 7.2 meV/f.u. than the FE state. Interestingly, we find that the cooperative coupling between A-site molecules and B-site Pb^{2+} ions is essential to stabilizing the FE state over the AFE state. This can be demonstrated in two aspects. Using the model Hamiltonian (see eq 1) and the corresponding parameters in Table S1 of the Supporting Information, one can show that the FE state will be less stable than the AFE state by 140.4 (or 26.0) meV/f.u. if the FE mode R_{BA} (or Γ_5^-) is set to 0, while the amplitudes of other three modes are set to 1. Besides, the indispensability of both R_{BA} and Γ_5^- modes to the ferroelectricity can also be demonstrated through direct DFT calculations. If one fully relaxes an initial structure in which the R_{BA} mode is initially set to 0 while the other three modes to 1, the Pb^{2+} ions will move back to the octahedral centers and the structure turns into the AFE state. Moreover, if we move the Pb^{2+} ions to octahedral centers of the FE structure and optimize all the other atomic positions while keeping the Pb^{2+} ions at octahedral centers using a modified VASP code (see section I of the Supporting Information), we can obtain a FE structure without any Pb FE displacements. The total energy of the FE state without Pb FE displacements turns out to be higher than that of the AFE state. The reason why displacements of Pb^{2+} ions help to lower the energy is that the empty 6p orbitals of lone-pair Pb^{2+} ions could form better covalent bonds with filled 3p orbitals of neighboring Cl^- ions,⁴⁸ similar to the second-order Jahn–Teller effect responsible for the ferroelectricity in usual inorganic ferroelectrics (e.g., BaTiO_3). Furthermore, we performed additional calculations on inorganic perovskite Cs_2PbCl_4 and HOIP $(\text{CHA})_2\text{PbBr}_4$ monolayers (see section IX of the Supporting Information); the results not only verify the essential of the cooperative coupling to the ferroelectricity in BA_2PbCl_4 monolayer but also demonstrate its generality. Our finding helps to resolve the debate on the role played by an A-site organic molecule and a B-site metal ion on the ferroelectricity in HOIPs.

It was found experimentally that there is no ferroelectricity in BA_2PbBr_4 and BA_2PbI_4 ^{18,30} in contrast to the case of BA_2PbCl_4 . We replace the Cl ligand with Br and I and calculate the energy difference between the AFE and FE states ($\Delta E = E_{\text{AFE}} - E_{\text{FE}}$) after structural optimizations (see Table 1). One can see that our DFT calculations are consistent with the experiment results.^{18,30} Now we try to understand why the AFE state is favored in the BA_2PbBr_4 and BA_2PbI_4 monolayers. As shown in Table 1, we analyze the amplitudes of the distortion modes with different halogen ions from Cl to I. One can see that the amplitudes of the Γ_5^- mode of the FE structure decreases significantly with increasing atomic radius from Cl to

I. According to the energy terms shown in Table S1, the decrease of the Γ_5^- mode will weaken the coupling strength in FE state, resulting in the AFE ground state in BA_2PbBr_4 and BA_2PbI_4 (see Figure 3c,d). It is interesting to see whether BA_2PbF_4 with a lighter X^- ion has stronger ferroelectricity than BA_2PbCl_4 as the FE instability of the Pb ion increase from I to F due to the stronger Pauli repulsion between Pb^{2+} and heavier X^- ions.⁴⁹ To our best knowledge, there is no report on BA_2PbF_4 yet. Our DFT calculations predict that the BA_2PbF_4 monolayer is an insulator (see section X of the Supporting Information) and displays the FE ground state with a lower total energy than the AFE state by about 39.6 meV/f.u. (see Table 1) and a polarization about $7.32 \mu\text{C}/\text{cm}^2$, which is higher than that (about $5.65 \mu\text{C}/\text{cm}^2$) in the BA_2PbCl_4 monolayer. The cooperative coupling between A-site molecules and B-site Pb^{2+} ions is also crucial to the ferroelectricity in BA_2PbF_4 monolayer (as can be seen from Table S1 of the Supporting Information), similar to the BA_2PbCl_4 case.

To estimate the FE Curie temperature of BA_2PbCl_4 and BA_2PbF_4 monolayers, we perform Monte Carlo (MC) simulations with a Ising-like model (see section XI of the Supporting Information for details). In Figure S12, one can see that T_c for BA_2PbCl_4 monolayer is about 610 K, close to the experimental value (about 438 K).¹⁸ As for BA_2PbF_4 monolayer, T_c is estimated to be about 1700 K from the MC simulations. It is well-known that Ising model overestimates the T_c . To further confirm the higher FE T_c in BA_2PbF_4 monolayer, we perform first-principles molecular dynamics (MD) simulations on BA_2PbCl_4 and BA_2PbF_4 monolayers. In our MD simulations, we start from the initial FE state with the polarization along the b -axis, then we gradually increase the temperature. To characterize the stability of the FE state, we compute the average b component of C–N vector $[\bar{d}_b = \frac{1}{N}(\sum_i |\vec{d}_i| \cos \theta_i)]$, where \vec{d}_i and θ_i represent the i th C–N vector and the angle between the vector and the $+b$ direction, respectively] since the orientations of the C–N vectors are closely related to the electric polarization. Our MD simulations show the two FE monolayers are both stable at room temperature (see Figure S13 of the Supporting Information). We find that FE BA_2PbF_4 monolayer is still stable at 400 K in contrast to the FE BA_2PbCl_4 monolayer case (see Figure 4). Therefore, our MD simulations confirm that the BA_2PbF_4 monolayer has a higher FE T_c than the BA_2PbCl_4 monolayer.

To summarize, we carry out a systematic study on the mechanism of ferroelectricity in 2D HOIPs. To this end, we propose an exact, simple, and general method to calculate the coupling strength between different modes. Applying this new method to the typical 2D HOIP ferroelectric BA_2PbCl_4 , we reveal that there is a cooperative coupling between A-site organic molecules and the inorganic framework and this coupling is essential to the ferroelectricity in HOIPs. The cooperative coupling between organic molecules and inorganic framework not only explains the absence of ferroelectricity in BA_2PbBr_4 and BA_2PbI_4 but also predicts high Curie temperature ferroelectricity in 2D BA_2PbF_4 since the cooperative coupling decreases from F to I. The new ferroelectric mechanism involving the cooperative coupling proposed in our work is generally applicable to other HOIP ferroelectrics as we demonstrated for the $(\text{CHA})_2\text{PbBr}_4$ case. Our work not only sheds new light on the debates on the ferroelectricity in

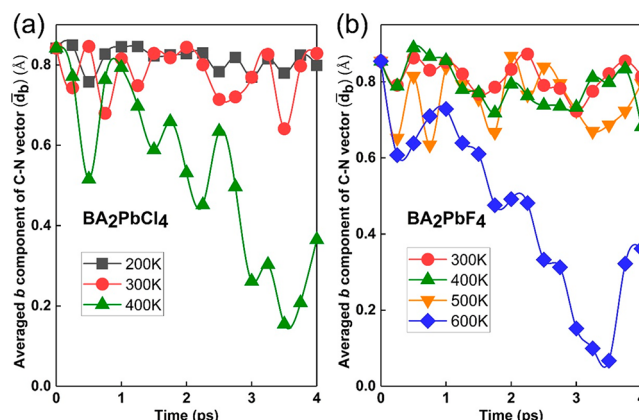


Figure 4. Thermal stability of the FE BA_2PbX_4 ($\text{X} = \text{Cl}, \text{F}$) monolayer. (a), (b) Fluctuation of the averaged b component of the C–N vector as a function of simulation time for FE BA_2PbCl_4 and BA_2PbF_4 monolayers, respectively.

HOIPs such as MAPbI_3 but also provides a guideline to design 2D multifunctional HOIP ferroelectrics.

■ ASSOCIATED CONTENT

Supporting Information

The Supporting Information is available free of charge at <https://pubs.acs.org/doi/10.1021/acs.nanolett.1c00395>.

Computational methods, ground state of bulk BA_2PbCl_4 , construction of thin films from bulk BA_2PbCl_4 , ground state of bilayer BA_2PbCl_4 , ground state of monolayer BA_2PbCl_4 , electric polarization of monolayer BA_2PbCl_4 , mode coupling for monolayer BA_2PbCl_4 and a table of energy contributions, mode decomposition for the AFE state of monolayer BA_2PbCl_4 , verifying the generality of the cooperative coupling mechanism including a phonon spectrum, band structure of monolayer BA_2PbF_4 , Monte Carlo simulations for monolayer BA_2PbX_4 , and molecular dynamics simulations for monolayer BA_2PbX_4 , configurations and structures, and FE Curie temperature graphs (PDF)

■ AUTHOR INFORMATION

Corresponding Author

Hongjun Xiang – Key Laboratory of Computational Physical Sciences (Ministry of Education), State Key Laboratory of Surface Physics, and Department of Physics, Fudan University, Shanghai 200433, People's Republic of China; Shanghai Qizhi Institution, Shanghai 200232, People's Republic of China; Collaborative Innovation Center of Advanced Microstructures, Nanjing 210093, People's Republic of China; orcid.org/0000-0002-9396-3214; Email: hxiang@fudan.edu.cn

Authors

Yali Yang – Key Laboratory of Computational Physical Sciences (Ministry of Education), State Key Laboratory of Surface Physics, and Department of Physics, Fudan University, Shanghai 200433, People's Republic of China; Shanghai Qizhi Institution, Shanghai 200232, People's Republic of China

Feng Lou – Key Laboratory of Computational Physical Sciences (Ministry of Education), State Key Laboratory of Surface Physics, and Department of Physics, Fudan

University, Shanghai 200433, People's Republic of China;
Shanghai Qizhi Institution, Shanghai 200232, People's
Republic of China

Complete contact information is available at:

<https://pubs.acs.org/10.1021/acs.nanolett.1c00395>

Notes

The authors declare no competing financial interest.

ACKNOWLEDGMENTS

This work is supported by the National Natural Science Foundation of China (Grants No. 11825403 and No. 11804138), the Qing Nian Ba Jian Program, and Shanghai Super Postdoctoral Incentive Program. The authors also acknowledge useful discussions with Dr. Changsong Xu and Dr. Yueyu Zhang.

REFERENCES

- (1) Stranks, S. D.; Eperon, G. E.; Grancini, G.; Menelaou, C.; Alcocer, M. J.; Leijtens, T.; Herz, L. M.; Petrozza, A.; Snaith, H. J. Electron-hole diffusion lengths exceeding 1 micrometer in an organometal trihalide perovskite absorber. *Science* **2013**, *342* (6156), 341–344.
- (2) Xing, G.; Mathews, N.; Sun, S.; Lim, S. S.; Lam, Y. M.; Gratzel, M.; Mhaisalkar, S.; Sum, T. C. Long-range balanced electron- and hole-transport lengths in organic-inorganic $\text{CH}_3\text{NH}_3\text{PbI}_3$. *Science* **2013**, *342* (6156), 344–347.
- (3) Shi, D.; Adinolfi, V.; Comin, R.; Yuan, M.; Alarousu, E.; Buin, A.; Chen, Y.; Hoogland, S.; Rothenberger, A.; Katsiev, K.; Losovyj, Y.; Zhang, X.; Dowben, P. A.; Mohammed, O. F.; Sargent, E. H.; Bakr, O. M. Low trap-state density and long carrier diffusion in organolead trihalide perovskite single crystals. *Science* **2015**, *347* (6221), 519–522.
- (4) Zhu, H.; Fu, Y.; Meng, F.; Wu, X.; Gong, Z.; Ding, Q.; Gustafsson, M. V.; Trinh, M. T.; Jin, S.; Zhu, X. Y. Lead halide perovskite nanowire lasers with low lasing thresholds and high quality factors. *Nat. Mater.* **2015**, *14* (6), 636–642.
- (5) Xing, G.; Mathews, N.; Lim, S. S.; Yantara, N.; Liu, X.; Sabba, D.; Gratzel, M.; Mhaisalkar, S.; Sum, T. C. Low-temperature solution-processed wavelength-tunable perovskites for lasing. *Nat. Mater.* **2014**, *13* (5), 476–480.
- (6) Liu, Y.; Collins, L.; Proksch, R.; Kim, S.; Watson, B. R.; Doughty, B.; Calhoun, T. R.; Ahmadi, M.; Ievlev, A. V.; Jesse, S.; Retterer, S. T.; Belianinov, A.; Xiao, K.; Huang, J.; Sumpter, B. G.; Kalinin, S. V.; Hu, B.; Ovchinnikova, O. S. Chemical nature of ferroelastic twin domains in $\text{CH}_3\text{NH}_3\text{PbI}_3$ perovskite. *Nat. Mater.* **2018**, *17* (11), 1013–1019.
- (7) Ye, H. Y.; Tang, Y. Y.; Li, P. F.; Liao, W. Q.; Gao, J. X.; Hua, X. N.; Cai, H.; Shi, P. P.; You, Y. M.; Xiong, R. G. Metal-free three-dimensional perovskite ferroelectrics. *Science* **2018**, *361* (6398), 151–155.
- (8) Wang, Z. X.; Zhang, H.; Wang, F.; Cheng, H.; He, W. H.; Liu, Y. H.; Huang, X. Q.; Li, P. F. Superior transverse piezoelectricity in a halide perovskite molecular ferroelectric thin film. *J. Am. Chem. Soc.* **2020**, *142* (29), 12857–12864.
- (9) Niesner, D.; Wilhelm, M.; Levchuk, I.; Osvet, A.; Shrestha, S.; Batentschuk, M.; Brabec, C.; Fauster, T. Giant Rashba splitting in $\text{CH}_3\text{NH}_3\text{PbBr}_3$ organic-inorganic perovskite. *Phys. Rev. Lett.* **2016**, *117* (12), 126401.
- (10) Kepenekian, M.; Robles, R.; Katan, C.; Saponi, D.; Pedesseau, L.; Even, J. Rashba and Dresselhaus effects in hybrid organic-inorganic perovskites: from basics to devices. *ACS Nano* **2015**, *9* (12), 11557–11567.
- (11) Kepenekian, M.; Even, J. Rashba and Dresselhaus couplings in halide perovskites: accomplishments and opportunities for spintronics and spin-orbitronics. *J. Phys. Chem. Lett.* **2017**, *8* (14), 3362–3370.
- (12) Smith, I. C.; Hoke, E. T.; Solis-Ibarra, D.; McGehee, M. D.; Karunadasa, H. I. A layered hybrid perovskite solar-cell absorber with enhanced moisture stability. *Angew. Chem., Int. Ed.* **2014**, *53* (42), 11232–11235.
- (13) Tsai, H.; Nie, W.; Blancon, J. C.; Stoumpos, C. C.; Asadpour, R.; Harutyunyan, B.; Neukirch, A. J.; Verduzco, R.; Crochet, J. J.; Tretiak, S.; Pedesseau, L.; Even, J.; Alam, M. A.; Gupta, G.; Lou, J.; Ajayan, P. M.; Bedzyk, M. J.; Kanatzidis, M. G. High-efficiency two-dimensional Ruddlesden-Popper perovskite solar cells. *Nature* **2016**, *536* (7616), 312–316.
- (14) Cao, D. H.; Stoumpos, C. C.; Farha, O. K.; Hupp, J. T.; Kanatzidis, M. G. 2D homologous perovskites as light-absorbing materials for solar cell applications. *J. Am. Chem. Soc.* **2015**, *137* (24), 7843–7850.
- (15) Liu, J.; Leng, J.; Wu, K.; Zhang, J.; Jin, S. Observation of internal photoinduced electron and hole separation in hybrid two-dimensional perovskite films. *J. Am. Chem. Soc.* **2017**, *139* (4), 1432–1435.
- (16) Dammak, T.; Koubaa, M.; Boukheddaden, K.; Bougzhala, H.; Mlayah, A.; Abid, Y. Two-dimensional excitons and photoluminescence properties of the organic/inorganic (4- $\text{FC}_6\text{H}_4\text{C}_2\text{H}_4\text{NH}_3$)₂[PbI_4] nanomaterial. *J. Phys. Chem. C* **2009**, *113* (44), 19305–19309.
- (17) Katan, C.; Mercier, N.; Even, J. Quantum and dielectric confinement effects in lower-dimensional hybrid perovskite semiconductors. *Chem. Rev.* **2019**, *119* (5), 3140–3192.
- (18) Liao, W. Q.; Zhang, Y.; Hu, C. L.; Mao, J. G.; Ye, H. Y.; Li, P. F.; Huang, S. D.; Xiong, R. G. A lead-halide perovskite molecular ferroelectric semiconductor. *Nat. Commun.* **2015**, *6*, 7338.
- (19) Ye, H. Y.; Liao, W. Q.; Hu, C. L.; Zhang, Y.; You, Y. M.; Mao, J. G.; Li, P. F.; Xiong, R. G. Bandgap engineering of lead-halide perovskite-type ferroelectrics. *Adv. Mater.* **2016**, *28* (13), 2579–2586.
- (20) Li, L.; Sun, Z.; Wang, P.; Hu, W.; Wang, S.; Ji, C.; Hong, M.; Luo, J. Tailored engineering of an unusual (C₄H₉NH₃)₂(CH₃NH₃)₂Pb₃Br₁₀ two-dimensional multilayered perovskite ferroelectric for a high-performance photodetector. *Angew. Chem., Int. Ed.* **2017**, *56* (40), 12150–12154.
- (21) Wu, Z.; Ji, C.; Li, L.; Kong, J.; Sun, Z.; Zhao, S.; Wang, S.; Hong, M.; Luo, J. Alloying n-Butylamine into CsPbBr₃ to give a two-dimensional bilayered perovskite ferroelectric material. *Angew. Chem., Int. Ed.* **2018**, *57* (27), 8140–8143.
- (22) Li, L.; Shang, X.; Wang, S.; Dong, N.; Ji, C.; Chen, X.; Zhao, S.; Wang, J.; Sun, Z.; Hong, M.; Luo, J. Bilayered hybrid perovskite ferroelectric with giant two-photon absorption. *J. Am. Chem. Soc.* **2018**, *140* (22), 6806–6809.
- (23) Yang, C. K.; Chen, W. N.; Ding, Y. T.; Wang, J.; Rao, Y.; Liao, W. Q.; Tang, Y. Y.; Li, P. F.; Wang, Z. X.; Xiong, R. G. The first 2D homochiral lead Iodide perovskite ferroelectrics: [R- and S-1-(4-Chlorophenyl)ethylammonium]₂PbI₄. *Adv. Mater.* **2019**, *31* (16), No. 1808088.
- (24) Li, L.; Liu, X.; Li, Y.; Xu, Z.; Wu, Z.; Han, S.; Tao, K.; Hong, M.; Luo, J.; Sun, Z. Two-dimensional hybrid perovskite-type ferroelectric for highly polarization-sensitive shortwave photodetection. *J. Am. Chem. Soc.* **2019**, *141* (6), 2623–2629.
- (25) Ji, C.; Wang, S.; Wang, Y.; Chen, H.; Li, L.; Sun, Z.; Sui, Y.; Wang, S.; Luo, J. 2D hybrid perovskite ferroelectric enables highly sensitive X-ray detection with low driving voltage. *Adv. Funct. Mater.* **2020**, *30* (30), No. 1905529.
- (26) Wang, S.; Liu, X.; Li, L.; Ji, C.; Sun, Z.; Wu, Z.; Hong, M.; Luo, J. An unprecedented biaxial trilayered hybrid perovskite ferroelectric with directionally tunable photovoltaic effects. *J. Am. Chem. Soc.* **2019**, *141* (19), 7693–7697.
- (27) Sha, T. T.; Xiong, Y. A.; Pan, Q.; Chen, X. G.; Song, X. J.; Yao, J.; Miao, S. R.; Jing, Z. Y.; Feng, Z. J.; You, Y. M.; Xiong, R. G. Fluorinated 2D lead Iodide perovskite ferroelectrics. *Adv. Mater.* **2019**, *31* (30), No. 1901843.
- (28) You, L.; Liu, F.; Li, H.; Hu, Y.; Zhou, S.; Chang, L.; Zhou, Y.; Fu, Q.; Yuan, G.; Dong, S.; Fan, H. J.; Gruverman, A.; Liu, Z.; Wang, J. In-plane ferroelectricity in thin flakes of van der Waals hybrid perovskite. *Adv. Mater.* **2018**, *30* (51), No. 1803249.

- (29) Shi, P. P.; Lu, S. Q.; Song, X. J.; Chen, X. G.; Liao, W. Q.; Li, P. F.; Tang, Y. Y.; Xiong, R. G. Two-dimensional organic-inorganic perovskite ferroelectric semiconductors with fluorinated aromatic spacers. *J. Am. Chem. Soc.* **2019**, *141* (45), 18334–18340.
- (30) Papavassiliou, G. C.; Mousdis, G. A.; Raptopoulou, C. P.; Terzis, A. Preparation and characterization of $[\text{C}_6\text{H}_5\text{CH}_2\text{NH}_3]_2\text{PbI}_4$, $[\text{C}_6\text{H}_5\text{CH}_2\text{CH}_2\text{SC}(\text{NH}_2)_2]_3\text{PbI}_5$ and $[\text{C}_{10}\text{H}_7\text{CH}_2\text{NH}_3]\text{PbI}_3$ organic-inorganic hybrid compounds. *Z. Naturforsch., B: J. Chem. Sci.* **1999**, *54* (11), 1405–1409.
- (31) Benedek, N. A.; Fennie, C. J. Hybrid improper ferroelectricity: a mechanism for controllable polarization-magnetization coupling. *Phys. Rev. Lett.* **2011**, *106* (10), 107204.
- (32) Elcombe, M. M.; Kisi, E. H.; Hawkins, K. D.; White, T. J.; Goodman, P.; Matheson, S. Structure determinations for $\text{Ca}_3\text{Ti}_2\text{O}_7$, $\text{Ca}_4\text{Ti}_3\text{O}_{10}$, $\text{Ca}_{3.6}\text{Sr}_{0.4}\text{Ti}_3\text{O}_{10}$ and a refinement of $\text{Sr}_3\text{Ti}_2\text{O}_7$. *Acta Crystallogr., Sect. B: Struct. Sci.* **1991**, *47*, 305–314.
- (33) Lobanov, M. V.; Greenblatt, M.; Caspi, E. A. N.; Jorgensen, J. D.; Sheptyakov, D. V.; Toby, B. H.; Botez, C. E.; Stephens, P. W. Crystal and magnetic structure of the $\text{Ca}_3\text{Mn}_2\text{O}_7$ Ruddlesden-Popper phase: neutron and synchrotron x-ray diffraction study. *J. Phys.: Condens. Matter* **2004**, *16* (29), S339–S348.
- (34) Crawford, M. K.; Subramanian, M. A.; Harlow, R. L.; Fernandez-Baca, J. A.; Wang, Z. R.; Johnston, D. C. Structural and magnetic studies of Sr_2IrO_4 . *Phys. Rev. B: Condens. Matter Mater. Phys.* **1994**, *49* (13), 9198–9201.
- (35) Balachandran, P. V.; Puggioni, D.; Rondinelli, J. M. Crystal-chemistry guidelines for noncentrosymmetric A_2BO_4 Ruddlesden-Popper oxides. *Inorg. Chem.* **2014**, *53* (1), 336–348.
- (36) Balachandran, P. V. Machine learning guided design of functional materials with targeted properties. *Comput. Mater. Sci.* **2019**, *164*, 82–90.
- (37) Benedek, N. A.; Rondinelli, J. M.; Djani, H.; Ghosez, P.; Lightfoot, P. Understanding ferroelectricity in layered perovskites: new ideas and insights from theory and experiments. *Dalton Trans.* **2015**, *44* (23), 10543–10558.
- (38) Hang, T.; Zhang, W.; Ye, H. Y.; Xiong, R. G. Metal-organic complex ferroelectrics. *Chem. Soc. Rev.* **2011**, *40* (7), 3577–3598.
- (39) Zhang, W.; Xiong, R. G. Ferroelectric metal-organic frameworks. *Chem. Rev.* **2012**, *112* (2), 1163–1195.
- (40) Wang, S.; Li, L.; Weng, W.; Ji, C.; Liu, X.; Sun, Z.; Lin, W.; Hong, M.; Luo, J. Trilayered lead chloride perovskite ferroelectric affording self-powered visible-blind ultraviolet photodetection with large zero-bias photocurrent. *J. Am. Chem. Soc.* **2020**, *142* (1), 55–59.
- (41) Wu, Z.; Liu, X.; Ji, C.; Li, L.; Wang, S.; Peng, Y.; Tao, K.; Sun, Z.; Hong, M.; Luo, J. Discovery of an above-room-temperature antiferroelectric in two-dimensional hybrid perovskite. *J. Am. Chem. Soc.* **2019**, *141* (9), 3812–3816.
- (42) Pickard, C. J.; Needs, R. J. Ab initio random structure searching. *J. Phys.: Condens. Matter* **2011**, *23* (5), 053201.
- (43) Jia, F.; Hu, S.; Xu, S.; Gao, H.; Zhao, G.; Barone, P.; Stroppa, A.; Ren, W. Persistent spin-texture and ferroelectric polarization in 2D hybrid perovskite Benzylammonium lead-halide. *J. Phys. Chem. Lett.* **2020**, *11* (13), 5177–5183.
- (44) Stroppa, A.; Jain, P.; Barone, P.; Marsman, M.; Perez-Mato, J. M.; Cheetham, A. K.; Kroto, H. W.; Picozzi, S. Electric control of magnetization and interplay between orbital ordering and ferroelectricity in a multiferroic metal-organic framework. *Angew. Chem., Int. Ed.* **2011**, *50* (26), 5847–5850.
- (45) Stroppa, A.; Barone, P.; Jain, P.; Perez-Mato, J. M.; Picozzi, S. Hybrid improper ferroelectricity in a multiferroic and magnetoelectric metal-organic framework. *Adv. Mater.* **2013**, *25* (16), 2284–2290.
- (46) Polyakov, A. O.; Arkenbout, A. H.; Baas, J.; Blake, G. R.; Meetsma, A.; Caretta, A.; van Loosdrecht, P. H. M.; Palstra, T. T. M. Coexisting ferromagnetic and ferroelectric order in a CuCl_4 -based organic-inorganic hybrid. *Chem. Mater.* **2012**, *24* (1), 133–139.
- (47) Gomez-Aguirre, L. C.; Pato-Doldan, B.; Stroppa, A.; Yanez-Vilar, S.; Bayarjargal, L.; Winkler, B.; Castro-Garcia, S.; Mira, J.; Sanchez-Andujar, M.; Senaris-Rodriguez, M. A. Room-temperature polar order in $[\text{NH}_4][\text{Cd}(\text{HCOO})_3]$ —a hybrid inorganic-organic compound with a unique perovskite architecture. *Inorg. Chem.* **2015**, *54* (5), 2109–2116.
- (48) Zhao, W. P.; Shi, C.; Stroppa, A.; Di Sante, D.; Cimpoesu, F.; Zhang, W. Lone-Pair-Electron-Driven Ionic Displacements in a Ferroelectric Metal-Organic Hybrid. *Inorg. Chem.* **2016**, *55* (20), 10337–10342.
- (49) Ravez, J. The inorganic fluoride and oxyfluoride ferroelectrics. *J. Phys. III* **1997**, *7* (6), 1129–1144.